Atomic Layer-by-Layer Thermoelectric Conversion in Topological Insulator Bismuth/Antimony Tellurides

Ji Ho Sung,[†,‡,⊥] Hoseok Heo,[†,‡,⊥] Inchan Hwang,[†,§] Myungsoo Lim,[∥] Donghun Lee,[†] Kibum Kang,[†] Hee Cheul Choi,[†,‡] Jae-Hoon Park,[‡,∥] Seung-Hoon Jhi,[∥] and Moon-Ho Jo*[,†,‡,§]

[†]Center for Artificial Low Dimensional Electronic Systems, Institute for Basic Science (IBS), Pohang University of Science and Technology (POSTECH), 77 Cheongam-Ro, Pohang 790-784, Korea

[‡]Division of Advanced Materials Science, Pohang University of Science and Technology (POSTECH), 77 Cheongam-Ro, Pohang 790-784, Korea

[§]Department of Materials Science and Engineering, Pohang University of Science and Technology (POSTECH), 77 Cheongam-Ro, Pohang 790-784, Korea

[∥]Department of Physics, Pohang University of Science and Technology (POSTECH), 77 Cheongam-Ro, Pohang 790-784, Korea

S Supporting Information

ABSTRACT: Material design for direct heat-to-electricity conversion with substantial efficiency essentially requires cooperative control of electrical and thermal transport. Bismuth telluride (Bi_2Te_3) and antimony telluride (Sb_2Te_3), displaying the highest thermoelectric power at room temperature, are also known as topological insulators (TIs) whose electronic structures are modified by electronic confinements and strong spin−orbit interaction in a-few-monolayers thickness regime, thus possibly providing another degree of freedom for electron and phonon transport at surfaces. Here, we explore novel thermoelectric conversion in the atomic monolayer steps of a-few-layer topological insulating Bi_2Te_3 (n-type) and Sb_2Te_3 (p-type). Specifically, by scanning photoinduced thermoelectric current imaging at the monolayer steps, we show that efficient thermoelectric conversion is accomplished by optothermal motion of hot electrons (Bi_2Te_3) and holes (Sb_2Te_3) through 2D subbands and topologically protected surface states in a geometrically deterministic manner. Our discovery suggests that the thermoelectric conversion can be interiorly achieved at the atomic steps of a homogeneous medium by direct exploiting of quantum nature of TIs, thus providing a new design rule for the compact thermoelectric circuitry at the ultimate size limit.

KEYWORDS: Thermoelectric Conversion, Photoinduced Thermoelectrics, Seebeck Effects, Topological Insulator, Bismuth Telluride, Antimony Telluride
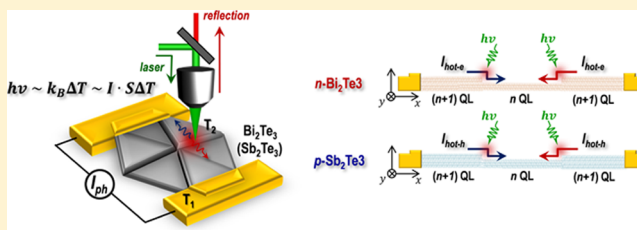
Thermoelectric conversion efficiency is determined by the thermopower (or Seebeck coefficient, S) of an electronic/thermal conductor, a measure of the magnitude of an induced thermoelectric voltage (ΔV) in response to an applied temperature difference (ΔK). Microscopically, in a conductor where the Fermi distribution is degenerated, the S is expressed by the Mott relation

$$S = \frac{\pi^2}{3}\left(\frac{k_B}{q}\cdot k_B T\right)\frac{d(\ln[\sigma(E)])}{dE}\bigg|_{E=E_F} \quad (1)$$

It describes the hot carrier conduction near the Fermi energy (E_F) through the band states or other localized states, where the differential conductivity, $d\sigma(E)/dE$, is expressed as the product of the derivatives of the carrier density (n) and mobility. Therein, local variation in the density of states ($dn(E)/dE$) near the E_F may contribute to the enhanced S. Typically, low dimensionality or inhomogeneous nanotexturing of thermoelectric materials have been attempted to tweak the

electronic structures and to independently engineer electron and phonon transport.[1−6] For example, it was reported that in bulk cubic chalcogenides such as Tl-doped PbTe via Tl-impurity states for the high temperature thermoelectric operation.[7−11] Bismuth telluride (Bi_2Te_3) shows an n-type semiconductor characteristic (with excessive Te) with a narrow gap (∼160 meV) with S of −(150−250) μV/K at room temperature, and they have been employed as the typical bulk thermoelectric materials for decades.[12−15] Similarly, antimony telluride (Sb_2Te_3) is a p-type narrow gap (∼100−280 meV) semiconductor with the room temperature S of ∼79 μV/K. Interestingly, they are also widely recognized as archetypal topological insulators (TIs), which are characterized by the topologically protected conducting surface-states forming a single spin-polarized Dirac cone on the bulk insulating interior
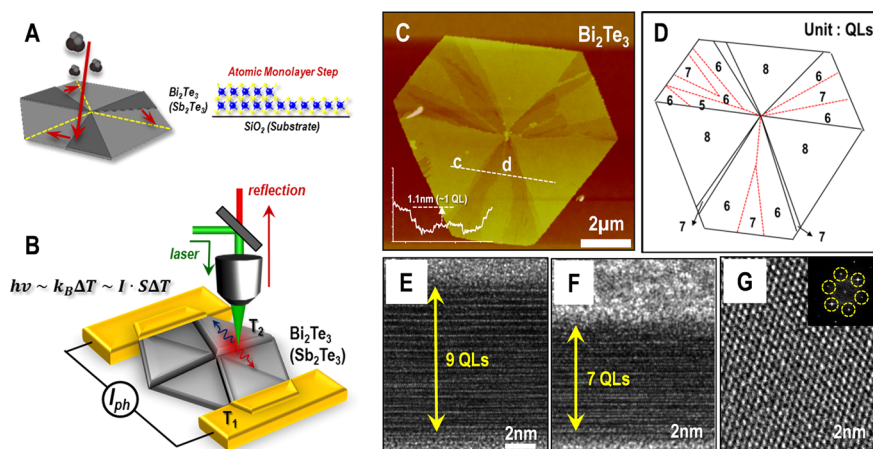
Figure 1. Monolayer-step terraced two-dimensional Bi_2Te_3 and Sb_2Te_3 crystals. (a) Gas-phase growth of atomic-step terraced 2D Bi_2Te_3 and Sb_2Te_3 crystals. (b) Our scanning optothermoelectric measurement scheme, where we simultaneously collect images of photoinduced current and optical reflectance as a function of the laser position. (c) Atomic force microscopy (AFM) surface image of Bi_2Te_3. (d) The quintuple layer (QL) numbers of (c). (e and f) Cross-sectional transmission electron microscope (TEM) images of each QLs of Bi_2Te_3. (g) In-plane TEM image of Bi_2Te_3.

due to strong spin−orbit coupling.[16−18] Recently, it has been invoked whether this topologically allowed surface conduction, from which the carrier backscattering is robustly suppressed, gives rise to a new thermoelectric conversion process, leading to a potentially much higher efficiency. Theoretical studies on such thermoelectric transport by Boltzmann, Landauer, and localization approaches predicted that hybridization of the top and bottom topological surface-states of a few monolayers Bi_2Te_3 lead to substantial enhancement of conversion efficiency.[19,20] They commonly share layered crystal structures in which the unit of Te−Bi(Sb)−Te−Bi(Sb)−Te hexagonal layers, called quintuple layers (QLs), is weakly coupled by van der Waals bonds between neighboring Te atoms. Therein, as the topological orders and electronic structures sensitively vary as a function of the QL numbers,[21] one may access to monolayer-resolved thermoelectric conversion processes by exploring the monolayer step boundaries of such TIs across the adjacent layers of different QL numbers. Here, we design an experiment to locally probe such individual monolayer steps with a focused laser as a local heater for their thermoelectric responses in a spatially resolved manner at the monolayer scale, as schematically shown in Figure 1a and b.

We intentionally form the monolayer (QL) step-terraced surface texture of two-dimensional (2D) Bi_2Te_3 and Sb_2Te_3 crystals, during a vapor transport synthesis, as shown in Figure 1c−g, characterized with an atomic force microscope and electron microscopy; also see Figure S1−2 of Supporting Information for detailed elemental and structure analyses. They are quite different from usual, atomically flat 2D crystals, in that within the triangularly or hexagonally faceted 2D crystals of typically ∼20−30 μm in size, the inner segments of different thickness of 4−12 QLs are in-plane symmetrically terraced over one or two QL steps.

Figure 1b and 2a illustrate our scanning photoinduced thermoelectric current (SThEC) probe with which the focused laser of a given wavelength (532 nm) and intensity is raster-scanned over the monolayer steps of the ohmic contacted, 2D Bi_2Te_3 and Sb_2Te_3 crystals. At the spatial resolution of the optical diffraction limit, the photoexcited current (I_{ph}) at a given spot is collected to the electrodes as a function of the laser-illumination position and forms a I_{ph} scanning images.[22,23] Simultaneously, we also collect the optical reflectance through
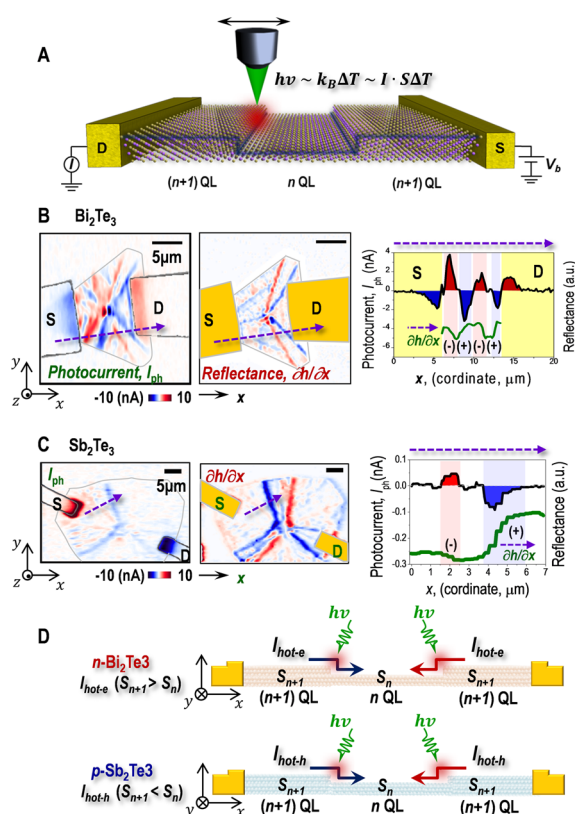

Figure 2. Scanning photoinduced thermoelectric current (SThEC) imaging on terraced two-dimensional Bi_2Te_3 and Sb_2Te_3 crystals. (a) Schematics of scanning optothermoelectric current imaging on the atomic monolayer steps. As a general working principle, focal laser heating induces thermal broadening near the E_F and produces either positive or negative current, depending on the carrier type (the relative E_F position). (b) (left) SThEC and (middle) the differential surface height h ($\partial h/\partial x$) image to the arrow direction. The red contour represents the thick-to-thin h transition at the step, and the blue one for the thin-to-thick transition. (right) The line profiles of SThEC and $\partial h/\partial x$ in the arrow direction. (c) The same of (b) for Sb_2Te_3. d The summary of b and c for the spatial changes in the I_{ph} directions.

the input lens to construct the scanning reflectance images, which is sensitive enough to resolve the monolayer surface

height (h) variation (Supporting Information Figure S3). Focal light absorption induces the local heating, creating a thermoelectric voltage difference along the induced temperature gradient. This thermoelectric voltage in turn drives the steady-state diffusion current between an illuminating spot and the collecting electrodes by opto-thermoelectric conversion, as $h\nu \sim k_B\Delta T \sim I_{ph}\cdot S\Delta T$. We note that the sign and magnitude of the observed, thermoelectric I_{ph} is principally determined by the type and concentration of the majority carriers of the responsible channels, that is, electrons for n-Bi$_2$Te$_3$ and holes for p-Sb$_2$Te$_3$. This contrasts to usual photovoltaic effects, by which we would have collected the same sign of the I_{ph}, particularly at the contact, due to interfacial band-bending, regardless of the majority carrier type; Bi$_2$Te$_3$ and S$_b$2Te$_3$ have similar electron affinity of 4.1−4.5 and 4.15 eV with small energy band gap of ∼200 and 280 meV;[6,24] thus, the relative positions of Fermi level with respect to the Cr/Au metal are expected to be similar, producing the same I_{ph} sign. Figure 2b and c are such SThEC images collected on our 2D QL-step terraced Bi$_2$Te$_3$ and Sb$_2$Te$_3$ crystals at the zero bias-voltage (V_b) with the corresponding differential reflectance images, showing the h variation. Here, we emphasize two main observations among others. First, it is most striking that the I_{ph} is inhomogeneous within both Bi$_2$Te$_3$ and Sb$_2$Te$_3$ channels and is abruptly modulated in its sign and magnitude at the local QL steps. Second, we observed that the strong I_{ph} is clearly imprinted underneath the channel-electrode overlapped area at source and drain electrodes, whose sign is opposite in Bi$_2$Te$_3$ and Sb$_2$Te$_3$. The second observation can be attributed to photoinduced thermovoltage generation at the metal junctions via thermal motions of the majority carriers (electrons for n-Bi$_2$Te$_3$ and holes for p-Sb$_2$Te$_3$) as further explained in Supporting Information Figure S6 and ref 25.[26]

We elaborate in more details on our principal observation of the I_{ph} modulation at the QL steps within individual 2D crystals, which is our primary focus. In order to quantitatively identify variation in the I_{ph} sign and magnitude with reference to variation in the layer numbers at individual monolayer steps (the first column of Figure 2b and c), we plot the differential h to the source-to-drain direction (x), $\partial h/\partial x$, from the acquired reflectance images as in the second column. Such one-to-one comparison in the third column, marked along the dotted lines, establishes an interesting deterministic correlation of the I_{ph} at each individual QL step. Specifically, in the reference to the current flowing direction, x, the I_{ph} signs for both Bi$_2$Te$_3$ and Sb$_2$Te$_3$ channels are positive for the thick-to-thin layer transitions, that is, $\partial I_{ph}/\partial x > 0$ for $\partial h/\partial x < 0$, and vice versa for the thin-to-thick transitions, $\partial I_{ph}/\partial x < 0$ for $\partial h/\partial x > 0$. Note that the majority carriers, responsible for our observations, are electrons for n-Bi$_2$Te$_3$ and holes for p-Sb$_2$Te$_3$. We have measured more than 20 devices of such 2D Bi$_2$Te$_3$ and Sb$_2$Te$_3$ crystals and have reproducibly found the same I_{ph} variation patterns, as shown in Supporting Information Figure S5. For simple clarity, we depict the summary in Figure 2d for the spatial changes in the I_{ph} directions.

The spatial variation in the sign and magnitude of I_{ph}, observed at the QL steps, can be described in the current density (j_{ph}) relation of

$$\vec{j}_{ph} = \sigma(-\nabla V_b) + \sigma S(-\nabla T) \qquad (2)$$

where V_b is zero in this case and σ is the conductivity. The deterministic I_{ph} sign to the geometrical variation in the QL

numbers strongly suggests that the difference in S between the adjacent i and j layers, $\Delta S (= S_i - S_j)$, where i and j are the QL numbers is responsible for the observed I_{ph} modulation, as illustrated in Figure 2d. In Figure 3a, we modeled the spatial I_{ph}
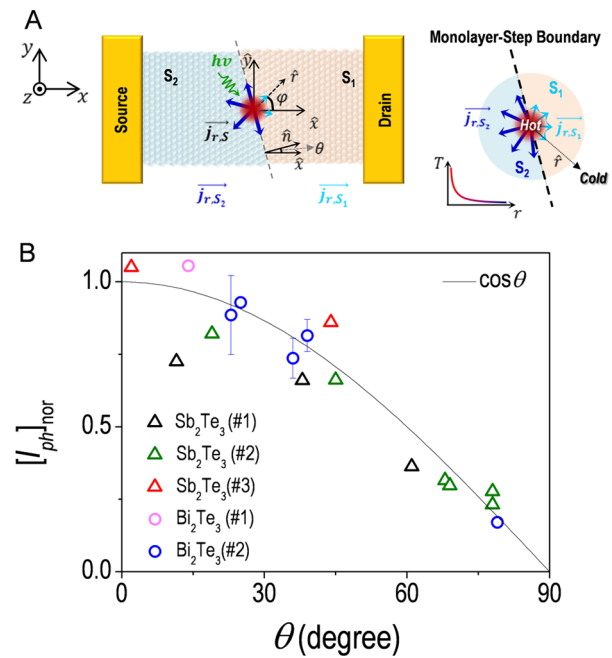

Figure 3. Spatial photoresponse at the step boundary in the 2D polar coordinate upon the focal light illumination at the coordinate origin. (a) Cross-sectional and plane views of the polar diversion of the current density ($\vec{j}$). (b) Angular dependence ($\vec{j}\cdot\hat{x}$) of the photoinduced thermoelectric current at the step boundary, collected from five different devices of Bi$_2$Te$_3$ and Sb$_2$Te$_3$.

response in the 2D polar coordinate ($\hat{r}, \boldsymbol{\varphi}$) upon the focal light illumination at the coordinate origin, where $\hat{r}$ and $\boldsymbol{\varphi}$ are the radial unit vector and rotation angle, for the hot carrier motions across the few monolayer steps. We set the step boundary normal vector, $\hat{n}$, which slants from the current flowing direction ($\hat{x}$) by the angle of θ. Therein, the effective electrical field ($\vec{E}$) generated by a temperature gradient (∇T) can be expressed by

$$\vec{E} = S\nabla T = S\Delta T\hat{r} \qquad (3)$$

Then, the total thermoelectric current density arising from the origin is given by

$$\vec{j} = \int_{\varphi=0}^{\varphi=2\pi} \vec{j}_r\, d\varphi = \int_{\varphi=0}^{\varphi=2\pi} \sigma S\Delta T\hat{r}\, d\varphi \qquad (4)$$

where

$$\vec{j}_r = \sigma\vec{E} = \sigma S\Delta T\hat{r}$$

This immediately suggests that $\vec{j}$ is only nonzero at the step boundary as

$$\vec{j} = \sigma(S_i - S_j)\Delta T\hat{r} \qquad (5)$$

Otherwise, $\vec{j}$ is zero elsewhere.

Finally, we get the net current component ($\vec{j}_x$), collected from the source to drain electrode, as

$$\vec{j}_x = \vec{j}\cdot\hat{x} = \sigma(S_i - S_j)\Delta T\hat{n}\cdot\hat{x} = \sigma(S_i - S_j)\Delta T\cos\theta \qquad (6)$$

This yields the angular dependence of the collected thermoelectric current, as $\vec{j}_x / \Delta S_{i,j} \sim \cos \theta$. We plot the measured I_{ph} normalized with $\Delta S_{i,j}$, analyzed from our scanned I_{ph} images of both Bi_2Te_3 and Sb_2Te_3 devices in Figure 3b, and found an excellent agreement with the model calculation for the angular dependence. This also precludes a possibility that ∇T in eq 2 is the governing factor for the I_{ph} variations; otherwise it would have a simple ∇T function over the distance from the local heating spots and the electrodes in the I_{ph} magnitude with the same I_{ph} sign; see Supporting Information Figure S7 for the laser-induced ΔT estimation.

Substantial difference between S_i and $S_{i\pm1}$ at the monolayer steps strongly suggests that the electronic structures near the E_F of our Bi_2Te_3 and Sb_2Te_3 2D crystals are modified at the step boundary in a nontrivial manner.[27−29] Indeed, the electronic structures of Bi_2Te_3 and Sb_2Te_3 in the few QL regimes are altered by (i) electronic energy confinements due to the finite size-effects, manifested at the band edges, that is, 2D subbands, and (ii) the emergence of topological surface-states within the bulk energy band-gaps.[30−32] Thereby, upon the specific position of the E_F tuned by the dopant types and concentration, both (i) and (ii) contributions must play critical roles in determining the sign and magnitude of the $\Delta S_{i,j}$ in our 2D crystals. We have verified that Bi_2Te_3 is degenerately doped n-type (metallic) and Sb_2Te_3 is lightly doped p-type (semiconducting) as in Supporting Information Figure S4. Thus, we expect that variation in the 2D subbands and the topological surface states is reflected on our observations because they significantly alter the energy derivatives of the carrier density $(\partial n / \partial E)$ within the gaps or at the edges of the bulk parabolic conduction bands. For example, in Bi_2Te_3, the S is particularly sensitive near the conduction band edge due to electronic confinement. Meanwhile, in Sb_2Te_3, the S is modified with the presence of the topological surface-states that is linearly dispersed within the gap. We tested this scenario by computing electronic structures of the 2D Bi_2Te_3 and Sb_2Te_3 crystals based on the density functional theory, where the QL number is ranged from 4 to 12, pertinent to our samples. We then calculated the relevant S values in the semiclassical Boltzmann transport limit, see Supporting Information Figure S8 for further calculation details. Figure 4a is the calculated electronic structures and the density of states of our 2D Bi_2Te_3 and Sb_2Te_3 crystals near the E_F. Note that the E_F levels are located at the bottom of the CB for the degenerate n-type Bi_2Te_3 and near the VB within the gap for the semiconducting p-type Sb_2Te_3, as also consistent with the dR/dT in Supporting Information Figure S4. In Figure 4a, it is found that the maximum magnitude of the $\partial n / \partial E$, marked as the dotted lines, is registered above the E_F of Bi_2Te_3 and below the E_F of Sb_2Te_3. At the constant scattering rate upon varying QL numbers, the $|S|$ is linearly proportional to the $\partial n / \partial E$ by the Mott relations. Specifically, in the n-type Bi_2Te_3, the number of the 2D subbands increases with increasing the QL numbers at the CB edge, resulting in the substantially enhanced S. Meanwhile, in the p-type Sb_2Te_3, the $|S|$ is decreasing in the QL range of 4−8, upon closing the gap formed by the topological surface-states. At the QL range over 12, the $|S|$ is calculated to approach to the bulk value. Figure 4b summarizes such QL number-dependent $|S|$ variation for our 2D Bi_2Te_3 and Sb_2Te_3 crystals, see also Supporting Information Figure S9. This is in turn consistent with variation in the I_{ph} sign and magnitude at the QL steps between adjacent i and j layers of Bi_2Te_3 and Sb_2Te_3, which can be plugged to extract the S by the relation from eq 2
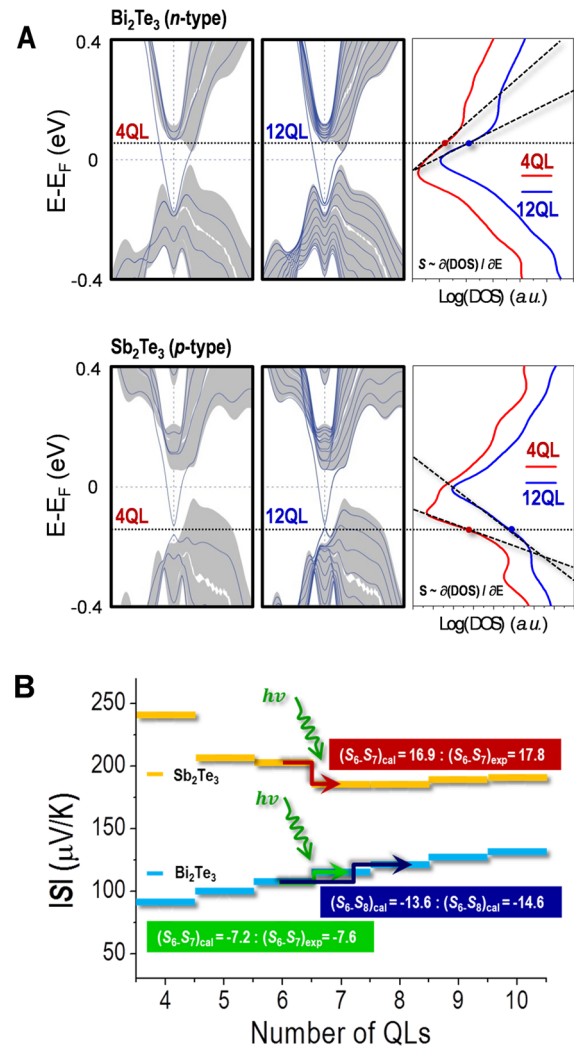

Figure 4. Efficient thermoelectric conversion by 2D subbands and topological surface states in few QL Bi_2Te_3 and Sb_2Te_3 crystals. (a) Band structures and the density of states near the E_F of Bi_2Te_3 and Sb_2Te_3 in our study. (b) The ΔS at the few QL steps of Bi_2Te_3 and Sb_2Te_3 from both first-principle calculations and our experiments as a function of the QL number.

$$S_i - S_j = \frac{I_{ph} \cdot R}{\Delta T} \tag{7}$$

We have quantitatively analyzed individual QL-step junctions at the Bi_2Te_3 7-to-6 and 8-to-6 layers junction and Sb_2Te_3 6-to-7 layers junction, from which we collected the peak I_{ph} at the individual steps. Consequently, we get the $(S_{6QL} - S_{7QL})$ and $(S_{6QL} - S_{8QL})$ of −7.6 and −14.6 $\mu V/K$ for Bi_2Te_3 and the $(S_{6QL} - S_{7QL})$ of 17.8 for Sb_2Te_3, respectively. These values agree well with the calculated values of −7.2, −13.6, and 16.9 $\mu V/K$, respectively. We note that atomic scale scanning probes such as a scanning tunneling microscopy/spectroscopy and conducting atomic force microscopy can directly measure the local S, as well as local electronic structures on epitaxial graphene.[33,34] We expect that a good heteroepitaxial combination of our monolayer stepped 2D Bi_2Te_3/Sb_2Te_3 2D crystals and conducting layers may be served for such direct probe techniques.

Strong photoresponse at the atomic layer boundaries, arising from hot carrier motions through 2D subbands and topological

surface states, is a rare example as direct probing of quantum nature at the macroscopic scale at room temperature.[22,35−39] The outcome thermoelectric powers arising from the monolayer steps of n-type Bi_2Te_3 and p-type Sb_2Te_3, are readily as large as the values reported for their bulk counterparts, and this finding suggests that an atomic scale $p−n$ thermocouple unit can be available for efficient thermoelectric conversion. As often demonstrated in other atomic 2D materials such as graphenes and h-BN, manipulation of such atomic sheets for the large-area device platforms is technologically viable.[40,41] Therefore, our observations for efficient thermoelectric conversion at the monolayer steps of the 2D Bi_2Te_3 and Sb_2Te_3, as well as the coherent hot carrier motions,[42−44] suggest practical implications for the development of highly efficient thermoelectrics in the ultimate size limit.

Materials: Vapor Transport Synthesis of 2D Bi_2Te_3 and Sb_2Te_3 Crystals. The 2D Bi_2Te_3 and Sb_2Te_3 crystals of few QLs were grown by a vapor transport synthesis from solid powder precursors. High purity Bi_2Te_3 or Sb_2Te_3 powders were placed in alumina boats and were loaded in the center of a 12-in. hot-walled quartz-tube furnace. SiO_2 (300 nm)/Si wafers as the growth substrates were also placed at the 10 cm downstream from the tube center considering the temperature gradient along the tube furnace. Prior to heating, the furnace was evacuated to 10^{-3} Torr and was purged with the high-purity nitrogen (N_2) to eliminate residual oxygen for 30 min. Then, the furnace was heated to 530 °C (for Sb_2Te_3) or 540 °C (for Bi_2Te_3) for 30 min at the 5 sccm of high purity argon (Ar) flow as a carrier gas under the total pressure of 0.1 Torr.

Methods: Scanning Thermoelectric Current (SThEC) Imaging. For the spectral photocurrent measurements, we used a broadband supercontinuum laser (450 nm $\leq \lambda \leq$ 2000 nm) combined with a monochromator for the high resolution spectra. During the wavelength scanning, photocurrent is measured by a lock-in technique with the chopper frequency of 10 kHz and subsequently normalized to the photon flux. The chopped laser beam is focused by microscopic lens (NA = 0.8) and illuminates the NW channel region of devices.

■ ASSOCIATED CONTENT

Ⓢ Supporting Information

Atomic layer-by-layer thermoelectric conversion in topological insulator bismuth/antimony tellurides. This material is available free of charge via the Internet at http://pubs.acs.org.

■ AUTHOR INFORMATION

Corresponding Author
*M.-H. Jo. E-mail: mhjo@postech.ac.kr.
Author Contributions
[⊥]These authors contributed equally to this work.
Notes
The authors declare no competing financial interest.

■ ACKNOWLEDGMENTS

■ REFERENCES

(1) Mahan, G. D.; Sofo, J. O. The best thermoelectric. *Proc. Natl. Acad. Sci.U. S. A.* 1996, 93, 7436−7439.

(2) Venkatasubramanian, R. E.; Colpitts, S. T.; O'Quinn, B. Thin-film thermoelectric devices with high room-temperature figures of merit. *Nature* 2001, 413, 597−602.

(3) Majumdar, A. Thermoelectricity in semiconductor nanostructures. *Science* 2004, 303, 777−778.

(4) Poudel, B.; et al. High-thermoelectric performance of nanostructured bismuth antimony telluride bulk alloys. *Science* 2008, 320, 634−638.

(5) Snyder, G. J.; Toberer, E. S. Complex thermoelectric materials. *Nat. Mater.* 2008, 7, 105−114.

(6) Tritt, T. M. Holey and unholey semiconductors. *Science* 1999, 283, 804−805.

(7) Heremans, J. P.; et al. Enhancement of thermoelectric efficiency in PbTe by distortion of the electronic density of states. *Science* 2008, 321, 554−557.

(8) Liu, H.; et al. Copper ion liquid-like thermoelectrics. *Nat. Mater.* 2012, 11, 422−425.

(9) Lee, J.-H.; Wu, J.; Grossman, J. C. Enhancing thermoelectric power factor with highly mismatched isoelectronic doping. *Phys. Rev. Lett.* 2010, 104, 016602.

(10) Pei, Y.; et al. Convergence of electronic bands for high performance bulk thermoelectrics. *Nature* 2011, 473, 66−69.

(11) Hinsche, N. F.; Yavorsky, B. Y.; Mertig, I.; Zahn, P. Influence of strain on anisotropic thermoelectric transport in Bi_2Te_3 and Sb_2Te_3. *Phys. Rev. B: Condens. Matter Mater. Phys.* 2011, 84, 165214.

(12) Fleurial, J. P.; Gailliard, L.; Triboulet, R. Thermal properties of high quality single crystals of bismuth telluride − part I: experimental characterization. *J. Phys. Chem. Solids* 1988, 49, 1237−1247.

(13) *Thermoelectrics Handbook: Micro to Nano*; Rowe, D. M., Ed.; CRC Press: New York, 2006.

(14) Teweldebrhan, D.; Goyal, V.; Balandin, A. Exfoliation characterization of bismuth telluride atomic quintuples quasi-two-dimensional crystals. *Nano Lett.* 2010, 10, 1209−1218.

(15) Kong, D.; et al. Ambipolar field effect in the ternary topological insulator $(Bi_xSb_{1-x})_2Te_3$ by composition tuning. *Nat. Nanotechnol.* 2011, 6, 705−709.

(16) Hsieh, D.; et al. A tunable topological insulator in the spin helical dirac transport regime. *Nature* 2009, 460, 1101−1105.

(17) Zhang, H.; et al. Topological insulators in Bi_2Se_3, Bi_2Te_3 and Sb_2Te_3 with a single Dirac cone on the surface. *Nat. Phys.* 2009, 5, 438−442.

(18) Chen, Y. L.; et al. Experimental realization of a three-dimensional topological insulator, Bi_2Te_3. *Science* 2009, 325, 178−181.

(19) Ghaemi, P.; Mong, R. S. K.; Moore, J. E. In-plane transport and enhanced thermoelectric performance in thin films of the topological insulator Bi_2Te_3 and Bi_2Se_3. *Phys. Rev. Lett.* 2010, 105, 166603.

(20) Maassen, J.; Lundstrom, M. A computational study of the thermoelectric performance of ultrathin Bi_2Te_3 films. *Appl. Phys. Lett.* 2013, 102, 093103.

(21) Mclver, J. W.; Hsieh, D.; Steinberg, H.; Jarillo-Herrero, P.; Gedik, N. Control over topological insulator photocurrents with light polarization. *Nat. Nanotechnol.* 2012, 7, 96−100.

(22) Kim, C.-J.; Lee, H.-S.; Cho, Y.-J.; Kang, K.; Jo, M.-H. Diameter-dependent internal gain in ohmic Ge nanowire photodetectors. *Nano Lett.* 2010, 10, 2043−2048.

(23) Kim, C.-J.; et al. On-nanowire band-graded Si:Ge photodetectors. *Adv. Mater.* 2011, 23, 1025−1029.

(24) Zuev, Y. M.; et al. Diameter dependence of the transport properties of antimony telluride nanowires. *Nano Lett.* 2010, 10, 3037−3040.

(25) The spatial variation in the sign and magnitude of I_{ph} can be described in the current density (j_{ph}) relation of $\vec{J}_{ph} = \sigma\,(-\nabla V_b) + \sigma S(-\nabla T)$, where $E_b \equiv -\nabla V_b$ is the electrical field by the applied V_b and σ is the conductivity. The strong I_{ph} generation at the Bi_2Te_3−metal junctions at the zero V_b, in our second observation, was similarly reported from an n-type monolayer MoS_2 [ref 26]. It can be attributed

to the photoexcited electrons (the majority carrier) diffusion across the thermovoltage difference at the junction, set by the relation of $j_{ph} = \sigma \Delta S \Delta T = \sigma (S_{Bi_2Te_3} - S_{Au}) (T_{Bi_2Te_3} - T_{Au}) \sim \sigma S_{Bi_2Te_3} (T_{Bi_2Te_3} - T_{Au})$, where S_{Au} is negligible compared to $S_{Bi_2Te_3}$. Meanwhile, the opposite I_{ph} sign at the Sb$_2$Te$_3$-metal contact indicates that the responsible carriers are holes, which is also consistent with the gate-voltage (V_g) dependent I_{dark} modulation in Bi$_2$Te$_3$ and Sb$_2$Te$_3$, as in Supporting Information Figure S4. Our observation of the opposite I_{ph} signs in n-type Sb$_2$Te$_3$ and p-type Bi$_2$Te$_3$ leads to a conclusion that the I_{ph} generation at the channel-contact junction is not due to usual photovoltaic effects, by which otherwise we would have collected the same sign of the I_{ph} regardless of the majority carrier type, generated by an optical interband transition at a steady state. Instead, we suggest that it arises from the photoinduced ThE effects, as is further evidenced in the text.

(26) Buscema, M.; Barkelid, M.; Zwiller, V.; van der Zant, H. S. J.; Steele, G. A. Large and tunable photothermoelectric effect in single-layer MoS$_2$. *Nano Lett.* **2013**, *13*, 358−363.

(27) Xu, X.; Gabor, N. M.; Alden, J. S.; ven der Zande, A. M.; McEuen, P. L. Photo-thermoelectric effect at a graphene interface junction. *Nano Lett.* **2010**, *10*, 562−566.

(28) Gabor, N. M.; et al. Hot carrier-assisted intrinsic photoresponse in graphene. *Science* **2011**, *334*, 648−652.

(29) Song, J. C. W.; Rudner, M. S.; Marcus, C. M.; Levitov, L. S. Hot carrier transport and photocurrent response in graphene. *Nano Lett.* **2011**, *11*, 4688−4692.

(30) Zhang, Y.; et al. Crossover of the three-dimensional topological insulator Bi$_2$Se$_3$ to the two-dimensional limit. *Nat. Phys.* **2010**, *6*, 584−588.

(31) Li, Y.-Y.; et al. Intrinsic topological insulator Bi$_2$Te$_3$ thin films on Si and their thickness limit. *Adv. Mater.* **2010**, *22*, 4002−4007.

(32) Yazyev, O. V.; Moore, J. E.; Louie, S. G. Spin polarization and transport of surface states in the topological insulators Bi$_2$Se$_3$ and Bi$_2$Te$_3$ from first principles. *Phys. Rev. Lett.* **2010**, *105*, 266806.

(33) Park, J.; He, G.; Feenstra, R. M.; Li, A.-P. Atomic-Scale Mapping of Thermoelectric Power on Graphene: Role of Defects and Boundaries. *Nano Lett.* **2013**, *13*, 3269−3273.

(34) Cho, S.; et al. Thermoelectric imaging of structural disorder in epitaxial graphene. *Nat. Mater.* **2013**, *12*, 913−918.

(35) Hsieh, D.; et al. Selective probing of photoinduced charge and spin dynamics in the bulk and surface of a topological insulator. *Phys. Rev. Lett.* **2011**, *107*, 077401.

(36) Ghosh, S.; et al. Dimensional crossover of thermal transport in few-layer graphene. *Nat. Mater.* **2010**, *9*, 555−558.

(37) Sun, D.; et al. Ultrafast hot-carrier-dominated photocurrent in graphene. *Nat. Nanotechnol.* **2012**, *7*, 114−118.

(38) Inoue, J.; Tanaka, A. Photoinduced transistion between conventional and topological insulators in two-dimensional electronic systems. *Phys. Rev. Lett.* **2010**, *105*, 017401.

(39) Junck, A.; Refael, G.; von Oppen, F. Photocurrent response of topological insulator surface states. *Phys. Rev. B: Condens. Matter Mater. Phys.* **2013**, *88*, 075144.

(40) Kim, K. S.; et al. Large-scale pattern growth of graphene films for stretchable transparent electrodes. *Nature* **2009**, *457*, 706−710.

(41) Levendorf, M. P.; et al. Graphene and boron nitride lateral heterostructures for atomically thin circuitry. *Nature* **2012**, *488*, 627−632.

(42) Chiritescu, C.; et al. Ultralow thermal conductivity in disordered, layered WSe$_2$ crystals. *Science* **2007**, *315*, 351−353.

(43) Kong, D.; Cui, Y. Opportunities in chemistry and materials science for topological insulators and their nanostructures. *Nat. Chem.* **2011**, *3*, 845−849.

(44) Graham, M. W.; Shi, S.-F.; Ralph, D. C.; Park, J.; McEuen, P. L. Photocurrent measurements of supercollision cooling in graphene. *Nat. Phys.* **2013**, *9*, 103−108.